J. Fluid Mech. (2012), *vol.* 691, *pp.* 165–177.
doi:10.1017/jfm.2011.466

Soft catenaries

Ken Kamrin[1]† **and L. Mahadevan**[2]†

[1] Department of Mechanical Engineering, Massachusetts Institute of Technology, Cambridge, MA 01239, USA

[2] School of Engineering and Applied Sciences and Department of Physics, Harvard University, Cambridge, MA 02138, USA

(Received 31 July 2011; revised 22 September 2011; accepted 19 October 2011; first published online 8 December 2011)

Using the classical catenary as a motivating example, we use slender-body theory to derive a general theory for thin filaments of arbitrary rheology undergoing large combined stretching and bending, which correctly accounts for the nonlinear geometry of deformation and uses integrated state variables to properly represent the complete deformation state. We test the theory for soft catenaries made of a Maxwell fluid and an elastic yield-stress fluid using a combination of asymptotic and numerical analyses to analyse the dynamics of transient sagging and arrest. We validate our results against three-dimensional finite element simulations of drooping catenaries, and show that our minimal models are easier and faster to solve, can capture all the salient behaviours of the full three-dimensional solution, and provide physical insights into the basic mechanisms involved.

Key words: complex fluids, low-dimensional models, non-Newtonian flows

1. Introduction

The interplay between geometry and continuum physics is rooted in the origins of seemingly simple questions such as the shape of an inextensible hanging chain under its own weight, the catenary, which was one of the first nonlinear problems to be solved exactly nearly three centuries ago. In the time since then, there have been many developments that account for the role of elasticity (Wang & Watson 1982), viscosity (Teichman & Mahadevan 2003; Koulakis *et al.* 2008), and viscoelasticity (Roy, Mahadevan & Thiffeault 2006) on the shape and the flow of the catenary. Here we generalize previous analyses to derive a theory for the finite bending and stretching of filaments of arbitrary rheologies to characterize the dynamics of a soft catenary – the rheoalysoid.

While linearized bending theories that account for small inelastic effects such as creep deformation in polymers and metals exist (Hult 1966; Kraus 1980), they have not typically been generalized to the case of geometrically nonlinear deformations. In contrast, for simple Newtonian viscous fluids, there have been a number of recent developments which utilize slender-body approximations to permit larger deformations and track the competing effects of bending and stretching to the filament dynamics (Howell 1996; Ribe 2001; Teichman & Mahadevan 2003; Roy *et al.* 2006; Brochard-Wyart & de Gennes 2007; Le Merrer *et al.* 2008; Zylstra & Mitescu 2009). Here we

† Email addresses for correspondence: kkamrin@mit.edu, lm@seas.harvard.edu

generalize previous work on the viscous and viscoelastic catenary to an analysis of arbitrary non-Newtonian rheology, including both the effects of elasticity and plastic yielding. This description covers a broad range of constitutive behaviours including Maxwell and Voigt models, elastic fluids with shear-thinning or shear-thickening flow, as well as yield-stress fluids such as the Bingham or Herschel–Bulkley models. To accomplish this, we generalize the classical theory of Euler and Bernoulli for elastic filaments to a low-dimensional theory for the geometrically nonlinear deformation of thin filaments of complex materials with finite extensional strains, negligible shear deformations, and curvature-dominated cross-sectional strain variation, and then use it to treat two distinct constitutive models – a Maxwell fluid and a Bingham–Norton viscoplastic law. This allows us to analyse a potentially new geometrical assay for nonlinear material rheology by visualizing large catenary-like deformations applicable for materials that can be easily and rapidly extruded as a bridge between points (like shaving foam) or by stretching a small blob as in Roy *et al.* (2006). Since our analysis applies in plane-stress conditions, it can also represent a long sheet with a finite out-of-plane width. While our theory is capable of accounting for thinning, here we avoid any discussion of flow instabilities such as necking/fracture when three-dimensional effects can become important. We also neglect the effect of capillary forces by assuming that the dimensionless parameter that characterizes its role in creeping flows, the capillary number, satisfies $Ca = \eta U/\gamma \gg 1$ where η is the viscosity of the material, γ is the surface tension and U a characteristic velocity scale in the problem.

2. Mathematical formulation

2.1. *Balance of force and moments*

We start with a slender filament of initial length L, cross-sectional area A_0 ($A_0/L^2 \ll 1$), and second moment of inertia I_0 in the thickness direction z. We focus on the simple case where A_0 and I_0 are constant along the length; however, our filament theory applies equally well if we replace these with $A_0(x_0)$ or $I_0(x_0)$ for initially inhomogeneous filaments. The filament material has density ρ and is suspended between two level supports at $x = \pm L/2$. Under the influence of its own weight, the filament deforms, so that a material point originating at $(x_0, 0)$ on the centreline of the filament is displaced to $\boldsymbol{x}(x_0, t) = (x(x_0, t), y(x_0, t))$. The deflected shape of the filament centreline, parametrized by an instantaneous (current) arclength variable s (measured from some prescribed position for $s = 0$) can be described by the local tangent angle with the horizontal $\theta(s)$ (figure 1), so that the local tangent is $\boldsymbol{x}_s = \boldsymbol{t} = (\cos\theta, \sin\theta)$.

Along a cross-section, the resultant forces and torques can be decomposed into a tension $T(s)$, shear $N(s)$, and a moment $M(s)$. Then, the equations of motion for the filament are

$$\boldsymbol{t}\text{-direction force} \quad T_s - N\theta_s - \lambda g \sin\theta = \lambda \boldsymbol{t} \cdot \boldsymbol{x}_{tt}, \tag{2.1}$$

$$\boldsymbol{n}\text{-direction force} \quad N_s + T\theta_s - \lambda g \cos\theta = \lambda \boldsymbol{n} \cdot \boldsymbol{x}_{tt}, \tag{2.2}$$

$$\text{moment} \quad N = M_s. \tag{2.3}$$

We choose the reference configuration x_0 and t to be the independent variables for this problem to avoid complicated expressions for the material acceleration $\boldsymbol{x}_{tt}$. Using the fact that $\partial_s(.) = \partial_{x_0}(.)/s_{x_0}$, and expressing the mass per unit length in the deformed configuration $\lambda = \lambda_0/s_{x_0}$, where $\lambda_0 = \rho A_0$ is the mass/length in the original

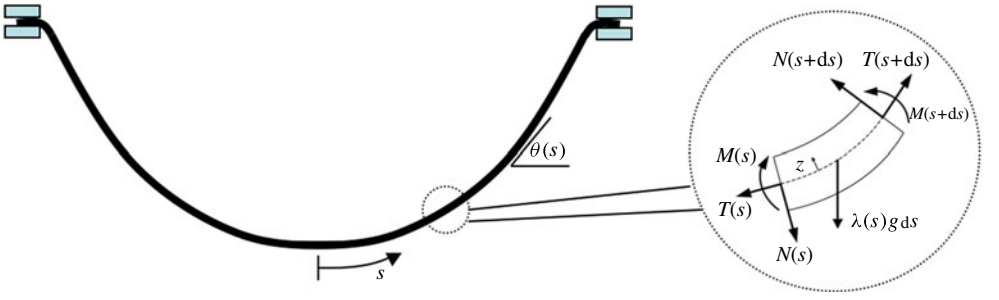

FIGURE 1. (Colour online available at journals.cambridge.org/flm) Definition of the arclength variable s and the angular variable θ. The close-up shows the forces and moments acting on a differential element of the filament, defined positive as drawn.

configuration, we may rewrite the equations of motion, after eliminating N, as

$$\boldsymbol{x}_{tt} = \frac{1}{\lambda_0}\begin{pmatrix} \cos\theta & \sin\theta \\ -\sin\theta & \cos\theta \end{pmatrix}\begin{pmatrix} T_{x_0} - M_{x_0}\theta_{x_0}/s_{x_0} - g\lambda_0 \sin\theta \\ M_{x_0x_0} - M_{x_0}s_{x_0x_0}/s_{x_0} + T\theta_{x_0} - g\lambda_0\cos\theta \end{pmatrix}. \tag{2.4}$$

This leads to an evolution law for the position $\boldsymbol{x}(x_0, t)$ in terms of $M(x_0, t)$, $T(x_0, t)$, and $\boldsymbol{x}(x_0, t)$, in combination with the identities

$$\left.\begin{aligned} s_{x_0} &= \sqrt{x_{x_0}^2 + y_{x_0}^2}, \quad s_{x_0x_0} = \frac{x_{x_0}x_{x_0x_0} + y_{x_0}y_{x_0x_0}}{s_{x_0}}, \quad \theta = \arctan\left(\frac{y_{x_0}}{x_{x_0}}\right), \\ \theta_{x_0} &= \frac{x_{x_0}y_{x_0x_0} - y_{x_0}x_{x_0x_0}}{s_{x_0}^2}. \end{aligned}\right\} \tag{2.5}$$

2.2. *A simple constitutive relation: linear Maxwell fluid*

To complete the equations of evolution for the motion of the filament (2.4), we require constitutive relations linking the various forces in terms of the kinematics of the filament. Invoking the classical Euler–Bernoulli beam assumptions that plane cross-sections of the filament remain planar, the only non-vanishing strain field is the axial strain $\epsilon(x_0, z, t)$ at a cross-section, which can be decomposed into two parts: the finite stretch of the centreline (measured as the true strain), and a z-dependent strain induced by the local curvature,

$$\epsilon(x_0, z, t) = \log(s_{x_0}) - \theta_{x_0}z. \tag{2.6}$$

For a simple Maxwell fluid where the tensile strain decomposes additively as the sum of an elastic strain ϵ^e and a viscous strain ϵ^p as $\epsilon(x_0, z, t) = \epsilon^e(x_0, z, t) + \epsilon^p(x_0, z, t)$, the constitutive relations are

$$\epsilon_t^p(x_0, z, t) = \frac{1}{\eta}\sigma(x_0, z, t), \tag{2.7}$$

$$\sigma(x_0, z, t) = E(\epsilon(x_0, z, t) - \epsilon^p(x_0, z, t)) \tag{2.8}$$

for a material with Young's modulus E and extensional flow viscosity η. As the filament stretches, it thins in the transverse plane to conserve volume, a phenomenon modelled by a uniform local areal contraction. Hence, the through-thickness area and inertia become

$$A(x_0, t) = A_0/s_{x_0}, \quad I(x_0, t) = I_0/s_{x_0}^2. \tag{2.9}$$

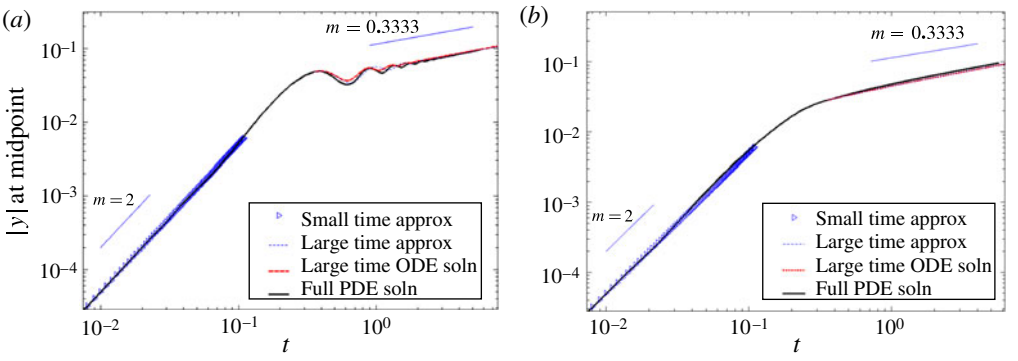

FIGURE 2. (Colour online) Comparisons of the asymptotic approximations for a Maxwell fluid filament to the numerical solution of the full PDE system (dimensionless units, $m =$ slope). (*a*) $\tau = 0.35$, (*b*) $\tau = 0.035$. (*a*,*b*) $\delta = 0.025$, $B = 3.3 \times 10^{-5}$. End (start) times for each regime given by the t_{low} (t_{high}) approximations in the text.

The resultant tension and moment are

$$T(x_0, t) = \int_A \sigma(x_0, z, t)\, \mathrm{d}a, \quad M(x_0, t) = \int_A \sigma(x_0, z, t) z\, \mathrm{d}a. \tag{2.10}$$

Expanding (2.10) using (2.8) and (2.6) to express T and M in terms of the kinematic quantities yields

$$T(x_0, t) = E(A(x_0, t)\log(s_{x_0}) - P(x_0, t)), \quad M(x_0, t) = -E(I(x_0, t)\theta_{x_0} + C(x_0, t)), \tag{2.11}$$

with P defined as $P(x_0, t) = \int_A \epsilon^p(x_0, z, t)\, \mathrm{d}a$ and $C(x_0, t) = \int_A \epsilon^p(x_0, z, t) z\, \mathrm{d}a$. The plastic stretch P and bend C evolve according to (2.7), which now implies

$$P_t(x_0, t) = \int_A \epsilon^p_t(z, x_0, t)\, \mathrm{d}a = T(x_0, t)/\eta, \quad C_t(x_0, t) = \int_A \epsilon^p_t(z, x_0, t) z\, \mathrm{d}a = M(x_0, t)/\eta. \tag{2.12}$$

Equations (2.4), (2.5), (2.9), (2.11) and (2.12) constitute a closed system of equations for the evolution of $(\boldsymbol{x}, \boldsymbol{x}_t, P, C)$. Given appropriate boundary/initial conditions, these laws govern the motion of the centreline of the filament, as well as the plastic strain state. Our theory may be trivially modified to account for pre-stressed filaments, reflected as a non-trivial initial condition for $P(x_0)$, $C(x_0)$, as done, for example, in Roy *et al.* (2006). Here, we choose $P(x_0) = C(x_0) = 0$ corresponding to a completely relaxed initial state of the filament.

Numerically solving this system for the case when the filament starts out horizontal with no initial velocity and with its ends clamped yields the evolving shape of the filament and thus its midpoint as a function of time, which is shown in figure 2 for two different relaxation times $\tau = \eta/E$. For each τ, we see that there are two distinct regimes for the evolution of the midpoint corresponding to the different force balances at play, associated with $t < t_{low}$ and $t > t_{high} > t_{low}$, which we analyse next.

In the small-deflection limit where $y/L \ll 1$ and $x - x_0 = U(x) \ll y$, we have

$$x \approx x_0,\ s \approx x,\ s_{x_0} - 1 \approx y_x^2/2 + U_x \ll 1,\ \theta \approx y_x \ll 1,\ A \approx A_0,\ I \approx I_0,\ \lambda \approx \lambda_0. \tag{2.13}$$

These approximations permit us to simplify (2.4) and (2.11) to

$$M_{xx} + Ty_{xx} = \lambda(y_{tt} + g), \quad T_x = 0, \tag{2.14}$$

$$T = E(A(y_x^2/2 + U_x) - P), \quad M = E(-Iy_{xx} - C). \tag{2.15}$$

Using (2.15) and (2.12), we can solve for T and M exactly using an integrating factor,

$$T = EA\mathrm{e}^{-Et/\eta}\int_0^t \mathrm{e}^{Et'/\eta}((y_x^2/2)_{t'} + U_{xt'})\,\mathrm{d}t', \quad M = -EI\mathrm{e}^{-Et/\eta}\int_0^t \mathrm{e}^{Et'/\eta}y_{xxt'}\,\mathrm{d}t'. \tag{2.16}$$

Using the fact that $T_x = 0$, we have

$$T(t) = \frac{2}{L}\int_0^{L/2} T\,\mathrm{d}x = \frac{2EA}{L}\mathrm{e}^{-t/\tau}\int_0^t \mathrm{e}^{t'/\tau}\left(\int_0^{L/2}(y_x^2/2)_{t'}\,\mathrm{d}x\right)\mathrm{d}t'. \tag{2.17}$$

Defining the dimensionless quantities $V = \eta/\rho\sqrt{gL^3}$, $\delta = h_0/L \ll 1$, $I/AL^2 = K\delta^2$, with K a constant, and the dimensionless variables $\bar{\tau} = \tau\sqrt{g/L}$, $\bar{t} = t\sqrt{g/L}$ and $(\bar{x}, \bar{y}) = (x, y)L$, we substitute (2.16), (2.17) into the first equation in (2.14) to obtain the initial/boundary value problem for the evolution of the shape of the filament,

$$-\delta^2 K\mathrm{e}^{-\bar{t}/\bar{\tau}}\int_0^{\bar{t}} \mathrm{e}^{t'/\bar{\tau}}y_{\bar{x}\bar{x}\bar{x}\bar{x}t'}\,\mathrm{d}t' + \bar{y}_{\bar{x}\bar{x}}\mathrm{e}^{-\bar{t}/\bar{\tau}}\int_0^{\bar{t}} \mathrm{e}^{t'/\bar{\tau}}\left(\int_0^{1/2}(\bar{y}_{\bar{x}}^2/2)_{t'}\,\mathrm{d}\bar{x}\right)\mathrm{d}t' = (\bar{y}_{\bar{t}\bar{t}} + 1)\bar{\tau}/2V, \tag{2.18}$$

$$\bar{y}(\pm 1/2, \bar{t}) = \bar{y}_{\bar{x}}(\pm 1/2, \bar{t}) = 0, \quad \bar{y}(\bar{x}, 0) = \bar{y}_{\bar{t}}(\bar{x}, 0) = 0. \tag{2.19}$$

We now drop the overbars. The above integro-differential equation differs from the corresponding form derived in Roy *et al.* (2006) for Oldroyd B fluid primarily by the presence of inertia and the continued coupling of the deformation to the stress relaxation through the two time integrals; physically, this corresponds to the dominance of extensional stresses that relax slowly, as compared to the case treated in Roy *et al.* (2006), where it is assumed that the shear stresses relax slowly. The first term on the left of (2.18) is due to the bending resistance of the filament, the next represents tensile stretching resistance, and both are balanced by inertial and gravitational body forces on the right. For small values of time, the free-fall effect dominates the bending and stretching terms: y and its space derivatives are initially small, and so is the bending term by virtue of being $O(\delta^2)$. Hence, up to some time t_{low}, dominant balance yields $y_{tt} + 1 = 0$, which can be solved for the midpoint deformation as $y(0, t) = -t^2/2$. At later times, $t > t_{high} > t_{low}$, the effect of inertia can be neglected as the tension dominates the still-negligible bending term. Letting $B \equiv 1/2V$, in this regime

$$y_{xx}\mathrm{e}^{-t/\tau}\int_0^t \mathrm{e}^{t'/\tau}\left(\int_0^{1/2}(y_x^2/2)_{t'}\,\mathrm{d}x\right)\mathrm{d}t' = \tau B. \tag{2.20}$$

An exact solution of (2.20) is $y(x, t) = (x^2 - 1/4)\phi(t)$ for $t = \tau\log\phi(t) + \phi(t)^3/9B$. This 'outer' solution neglects boundary layers of sharp bending near the supports, i.e. $y_x(\pm 1/2, t) \neq 0$. In the large time limit, neglecting the logarithmic viscoelastic relaxation term leads to the simple expression $\phi(t) = (9Bt)^{1/3}$ and the corresponding midpoint deflection relation $y(0, t) = -(9Bt)^{1/3}/4$, which is consistent with the behaviours in Teichman & Mahadevan (2003) and Roy *et al.* (2006).

When $t < t_{low}$ we simplify by considering a parabolic spatial dependence, implying $y(x, t) = 2t^2(x^2 - 1/4)$. The size of the tensile term corresponding to this deformation, i.e. the second term on the left of (2.18), is $16t^5\tau/3$. Similarly, the inertial term

is $|y_{tt}B\tau| = B\tau$. Setting the ratio of tensile to inertial terms, $16t^5/3B$, equal to some tolerance $\alpha \ll 1$ allows us to solve the resulting equation for t_{low}. Conversely, the long-time solution should be valid when its corresponding inertial term is less than α times the tensile contribution, ultimately giving $(B/3t_{high}^5)^{1/3}/6 = \alpha$ as a criterion for inferring t_{high}. In what follows, we approximate t_{low} and t_{high} using $\alpha = 1/15$. By visualizing an experiment, we could measure these times, respectively, by the point where the midpoint deflection ceases to be quadratic in time, and the point where a $1/3$ power law begins (possibly with oscillations thereof, discussed next).

When $t \approx t_{high}$ the competition between elasticity and 'residual' inertia can lead to underdamped oscillations of the filament. Assume for $t > t_{high}$ that the shape follows a perturbed version of the asymptotic shape, i.e. $y(x, t) = (x^2 - 1/4)(-(9Bt)^{1/3}/4 + \lambda f(t))$ for small λ and unknown function f. We substitute this into (2.18), neglect the $O(\delta^2)$ bending term, expand to $O(\lambda^1)$, and integrate the result from $x = 0$ to $1/2$ to get an equation for the evolution of the midpoint height. Keeping the three largest terms in the result leads to the following ordinary differential equation for f:

$$\tau f''' + f'' + 6\,(3t^2/B)^{1/3} f' = 0, \tag{2.21}$$

When $t \approx t_{high}$, (2.21) approximates to a linear constant-coefficient ordinary differential equation with the solution

$$f(t) \approx a_1 + a_2 \mathrm{e}^{-t/2\tau} \cos(Rt) + a_3 \mathrm{e}^{-t/2\tau} \sin(Rt) \tag{2.22}$$

for $R = (1/2\tau)\,(24\tau\,(3t_{high}^2/B)^{1/3} - 1)^{1/2}$.

Comparisons of the numerical solution of (2.21) and the approximate solution equation (2.22) with those of the complete system shown in figure 2 show that we can capture the different transients using this simplified theory. Our expression for the damped oscillations (2.22) gives an initial oscillation period of $2\pi/R$. Through our various formulae, η and E can be expressed in terms of R, t_{high}, and B, which can each be measured experimentally by visualizing the midpoint of the filament; this suggests an experimental procedure for measuring the Maxwell fluid properties η and E from a drooping filament.

2.3. *A non-Newtonian constitutive law: yield-stress materials*

To account for materials with a yield criterion or other kind of non-Newtonian flow behaviour, one must modify (2.12) and correctly account for the transition from elastic deformation to plastic flow, since now the time derivatives of P and C cannot be expressed directly in terms of T and M owing to the nonlinearity of the flow rule $\epsilon_t^p = \hat{\epsilon}_t^p(\sigma)$. In the thin filament limit of interest here, the variation in the extensional stress $\sigma(z, x_0, t)$ across the thickness is assumed linear in z, so that $\sigma(z) = \sigma_0 + \sigma_1 z$. Then the resultant tension and torque are given by

$$T = \int_A (\sigma_0 + \sigma_1 z)\,\mathrm{d}z\,\mathrm{d}y = \sigma_0 A, \quad M = \int_A (\sigma_0 + \sigma_1 z) z\,\mathrm{d}z\,\mathrm{d}y = \sigma_1 I. \tag{2.23}$$

Solving for σ_0 and σ_1 above, we substitute the resulting stress field into the flow rule to obtain

$$P_t = \int_A \hat{\epsilon}_t^p \left(\frac{T}{A} + \frac{M}{I} z\right) \mathrm{d}A, \quad C_t = \int_A \hat{\epsilon}_t^p \left(\frac{T}{A} + \frac{M}{I} z\right) z\,\mathrm{d}A, \tag{2.24}$$

completing our formulation for the plastic tension and plastic torque. For example, in the fundamental case of a Bingham–Norton fluid, an elastic perfectly viscoplastic

material with yield stress σ_Y and linear flow-rate dependence during plastic deformation, we have

$$\hat{\epsilon}_t^p(\sigma) = (\sigma - \text{sign}(\sigma)\sigma_Y)H(|\sigma| - \sigma_Y)/\eta, \tag{2.25}$$

where H is the Heaviside function.

Suppose a filament of this material has rectangular cross-section with initial thickness h_0 and out-of-plane width D_0. The stretching of the filament causes the cross-section to shrink according to the previous assumptions, i.e. $h = h_0/\sqrt{s_{x_0}}$, $D = D_0/\sqrt{s_{x_0}}$. In this geometry we have $A = hD$ and $I = h^3D/12$. Using (2.23), we write $\sigma(z) = (1/Dh)T + (12/Dh^3)Mz$. At each x_0, we first use this stress profile to solve directly for the positions z_H and z_L that characterize the boundaries of yielding zones, with the filament yielding in $-h/2 < z < z_L$ and $z_H < z < h/2$. It is often the case that $-h/2 = z_L$ (i.e. no yielding at the bottom edge), or $z_H = h/2$ (i.e. no yielding at the the top edge). Substituting (2.25) into (2.24) yields

$$P_t = \frac{1}{\eta}\left[\left(1 + \frac{z_L - z_H}{h}\right)T + 6M\frac{z_L^2 - z_H^2}{h^3} + \left(z_H - \frac{h}{2}\right)D\sigma_Y\text{sign}(6M + hT) + \left(z_L + \frac{h}{2}\right)D\sigma_Y\text{sign}(6M - hT)\right], \tag{2.26}$$

$$C_t = \frac{1}{\eta}\left[\left(1 - \frac{4(z_H^3 - z_L^3)}{h^3}\right)M + T\frac{z_L^2 - z_H^2}{2h} + \left(\frac{z_H^2}{2} - \frac{h^2}{8}\right)D\sigma_Y\text{sign}(6M + hT) + \left(\frac{z_L^2}{2} - \frac{h^2}{8}\right)D\sigma_Y\text{sign}(6M - hT)\right]. \tag{2.27}$$

Using (2.26), (2.27) in place of (2.12), together with (2.4), (2.5), (2.9), (2.11), and the initial/boundary conditions, we now have a closed system for the evolution of an elasto-viscoplastic filament with yield criterion.

3. Comparison of low-dimensional model with three-dimensional finite element simulations

We non-dimensionalize time and space by $(\tilde{x}, \tilde{y}, \tilde{x}_0) = (x, y, x_0)/L$ and $\tilde{t} = (t/L)\sqrt{E/\rho}$. To compute solutions of the one-dimensional reduced model, we encode the final equations in MATLAB, discretizing x_0 using $N \sim 40$ grid points to model half of the filament span. On each grid point we store six variables: x, y, x_t, y_t, P, and C. Centered first and second spatial derivatives are utilized and the system evolves as a $6N$ degree-of-freedom dynamical system, implemented using a fourth-order Runge–Kutta method.

The software ABAQUS/Explicit is used to perform the 3D finite element method (FEM) computations. For consistency, the FEM simulations use an end-clamping condition that keeps the cross-sectional plane vertical and fixes the location of its centre. We also mesh the filament with a one-element depth to capture the plane stress limit. For numerical reasons, we turn the gravity on in a non-abrupt fashion using a smooth ramp-up function that brings the gravity to its stated value over the time range $\tilde{t} = 0$ to some small value $\tilde{t} = g_{on}$.

3.1. *Three-dimensional constitutive law*

The constitutive law used in the finite-element simulations has a rigorous, three-dimensional, tensorial, finite-deformation, elasto-viscoplastic framework (Gurtin, Fried & Anand 2010). Under simple tension, the law reduces to the one-dimensional law

described in (2.25) with linear elastic response given by (2.8). The law enforces frame-indifference, material isotropy, and non-negative dissipation.

With $\boldsymbol{\sigma}$ the Cauchy stress tensor, $\boldsymbol{X}$ the initial (i.e. reference) position of a material point, $\boldsymbol{x}$ the current position, and the motion function $\boldsymbol{\chi}$ providing the correspondence between the two configurations – i.e. $\boldsymbol{x} = \boldsymbol{\chi}(\boldsymbol{X}, t)$ – the Bingham–Norton constitutive law is expressed as

$$\boldsymbol{F} = \frac{\partial \boldsymbol{\chi}}{\partial \boldsymbol{X}} \quad \text{deformation gradient,} \tag{3.1}$$

$$\boldsymbol{F} = \boldsymbol{F}^e \boldsymbol{F}^p \quad \text{Kroner–Lee decomposition of elasticity and plasticity,} \tag{3.2}$$

$$\boldsymbol{E}^e = \log(\sqrt{\boldsymbol{F}^{eT}\boldsymbol{F}^e}) \quad \text{elastic (Hencky) strain tensor,} \tag{3.3}$$

$$\boldsymbol{M} = (\det \boldsymbol{F}^e)\boldsymbol{F}^{e-1}\boldsymbol{\sigma}\boldsymbol{F}^e \quad \text{Mandel stress tensor,} \tag{3.4}$$

$$\tau = \sqrt{0.5\boldsymbol{M}' : \boldsymbol{M}'} \quad \text{equivalent shear stress,} \tag{3.5}$$

$$\boldsymbol{M} = \frac{E}{3(1-2\nu)}\mathrm{tr}(\boldsymbol{E}^e)\boldsymbol{1} + \frac{E}{1+\nu}\boldsymbol{E}^{e\prime} \quad \text{elasticity relation,} \tag{3.6}$$

$$\boldsymbol{L}^p = \frac{3}{\eta}H\left(\tau - \frac{\sigma_Y}{\sqrt{3}}\right)\left(\tau - \frac{\sigma_Y}{\sqrt{3}}\right)\frac{\boldsymbol{M}'}{|\boldsymbol{M}'|} \quad \text{constitutive law for Bingham viscoplasticity,} \tag{3.7}$$

$$\dot{\boldsymbol{F}}^p = \boldsymbol{L}^p \boldsymbol{F}^{p-1} \quad \text{evolution of plastic deformation gradient.} \tag{3.8}$$

In the above, primes denote the deviatoric part of a tensor and $\boldsymbol{A} : \boldsymbol{B} = \sum A_{ij}B_{ij}$. The quantities σ_Y, E, and η are, as before, the tensile yield stress, the Young's modulus, and the tensile flow viscosity. In addition, we take the elastic Poisson ratio $\nu = 0.45$. The plastic part of the deformation is assumed to be incompressible. These equations are augmented by the three-dimensional equation of motion $\nabla \cdot \boldsymbol{\sigma} + \rho \boldsymbol{g} = \rho(\mathrm{D}\boldsymbol{v}/\mathrm{D}t)$ to close the system.

3.2. *Comparisons*

Before we compare the results of our slender-body theory with that of three-dimensional simulations, it is useful to qualitatively identify the range of behaviours of a drooping viscoplastic filament. There are four natural parameters that describe the evolution of the filament:

$$\text{slenderness} \quad \delta = \frac{h_0}{L}, \quad \text{yield strain} \quad \epsilon_Y = \frac{\sigma_Y}{E}, \tag{3.9}$$

$$\text{gravity number} \quad G = \frac{g\rho L}{\sigma_Y}, \quad \text{viscous number} \quad V = \frac{\eta}{\rho\sqrt{gL^3}}. \tag{3.10}$$

We note there are two parameters that characterize the loading on the filament: a gravity number G, which defines the ratio of the self-stress on the filament due to its weight relative to the yield stress, and the viscous number V, which characterizes the ratio of a viscous 'velocity' $\eta/\rho L$ to a gravitational velocity $\sqrt{gL}$.

To understand the different regimes that can result during the sag of such a filament, we first consider the small deflection regime when we might assume a fully elastic solution where no part of the filament yields. We can understand this using scaling estimates. Letting H be the midpoint deflection, we balance the elastic bending energy of the filament $Eh_0^4H^2/L^3$ with the gravitational energy $\rho g h_0^2 LH$ to find that $H \sim \rho g L^4/Eh_0^2$. The maximum strain in the filament due to curvature then scales as $h_0H/L^2 \sim \rho g L^2/Eh_0$. For the filament not to yield anywhere, this strain must be less

than the yield strain, so that

$$2\delta > G, \tag{3.11}$$

where the prefactor arises from solving the linearized problem exactly.

In the opposite case, $\delta \leqslant G/2$, the filament yields at some location along its periphery. However, if the yield boundary does not penetrate all the way to the centre, the filament eventually stops flowing. To understand how a filament that experiences stress levels beyond σ_Y can first flow and then stop, settling into a sagged geometry, we consider the dynamics of the filament when it resembles that for a standard catenary with ends held at $(\pm L/2, 0)$, having the well-known form $y = a(\cosh(x/a) - \cosh(L/2a))$ parametrized by a length a, and negligible bending moments. The total deflection H obeys $H = a(\cosh(L/2a) - 1)$, which in the small deflection limit yields $a \approx L^2/8H$. The maximum tensile stress $\sigma_{max} = \rho g a \cosh(L/2a) = \rho g(H + a) \approx \rho g(H + L^2/8H)$ decreases to an approximate minimum of $\rho g L/\sqrt{2}$ at $H = L/\sqrt{8}$. Accordingly, a filament sagging plastically should eventually come to a stop if $\sigma_Y > \rho g L/\sqrt{2}$, or in dimensionless terms, $G < \sqrt{2}$. Combining this relation with the criterion for initial yielding gives us some bounds on the regime of arrested descent,

$$2\delta < G < \sqrt{2}. \tag{3.12}$$

Furthermore, by equating σ_{max} to σ_Y, we can compute the approximate deflection at which the filament should stop descending plastically, H_{stop}, by

$$H_{stop}/L = 1/2G - ((1/2G)^2 - 1/8)^{1/2}. \tag{3.13}$$

From a dynamical perspective, the arrested descent regime has two qualitative subcases corresponding to overdamped and underdamped limits. In the overdamped case, the inertia of the filament during the plastic descent is small compared to the viscous effects of the viscoplastic flow law so that the filament has an ever-decreasing, though non-zero, plastic flow rate that causes it to gradually approach a limiting static state. In the underdamped case, the filament has enough inertia to carry it a distance somewhat further than the limiting static configuration, leading to long-term elastic oscillations. Although it is difficult to derive an analytical expression to predict which of the over- and under-damped subcases will occur, it is clear that decreasing the value of the viscous number V will lead to a change from the overdamped to the underdamped case.

Lastly, in the regime of continual descent, the pull of gravity induces internal stresses persistently above yield and the filament droops continually for all time. The parameter range for continual descent is precisely that which lies outside the transient descent and no-yielding range, i.e.

$$\max(2\delta, \sqrt{2}) < G. \tag{3.14}$$

In figure 3(*a*), we show a phase diagram that characterizes these different phases.

We now examine numerical results of the full system in each regime. We fix $\delta = 0.03$, $g = 9.81$ m s^{-2}, $L = 20$ cm, $\rho = 1900$ kg m^{-3}, and $E = 4$ MPa. We vary G, ϵ_Y, V by varying σ_Y and η.

In the no-yielding regime, a comparison of the one-dimensional model to FEM provides a consistency check that the reduced-dimensional model is reasonable. To uphold inequality (3.11), we use $G = 0.01$. We simulate using $\epsilon_Y = 0.07$ and

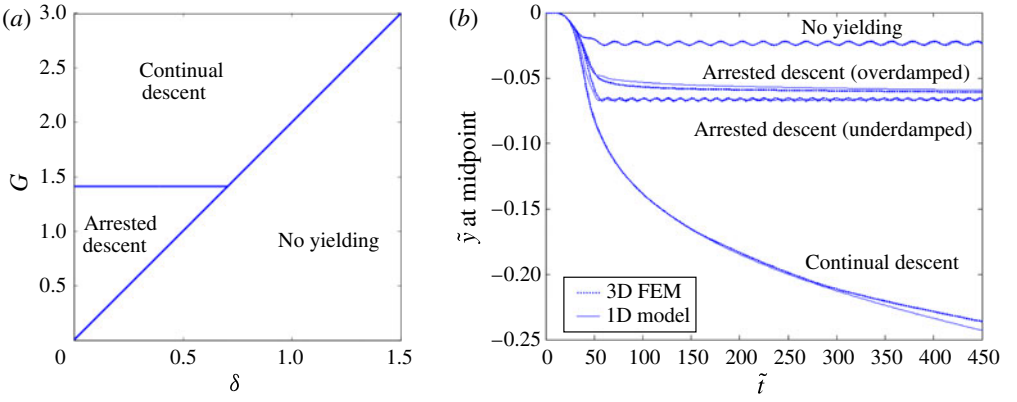

FIGURE 3. (Colour online) (*a*) Approximate phase diagram for qualitative behaviour of a catenary of viscoplastic material. (*b*) The vertical position of the filament midpoint as a function of time for parameters $(\delta, G, \epsilon_Y, V) = (0.03, 0.01, 0.07, -)$ (no yielding), $(0.03, 0.4, 0.002, 26)$ (transient descent, overdamped), $(0.03, 0.4, 0.002, 0.4)$ (transient descent, underdamped), $(0.03, 1.9, 0.0005, 26)$ (continual descent). The results of the reduced-dimensional one-dimensional model and the corresponding results under the fully meshed FEM simulation are simultaneously displayed.

arbitrary V. Both the one-dimensional and FEM simulations are dynamic with non-dissipative elastic response. As a result, after gravity ramps up, both solutions show long-term oscillations, demonstrating the reduced scheme's ability to correctly represent elastodynamics (see figure 3*b*, 'no yielding'). Moreover, as can be seen in figure 4(*b*), neither simulation indicates that any plastic deformation occurs, as predicted.

To compare results in the transient descent range, we choose $G = 0.40$ following inequality (3.12), and choose $\epsilon_Y = 2 \times 10^{-3}$. We perform tests using $V = 26$ and $V = 0.40$ to explore both the over- and under-damped cases respectively. As can be seen in figure 3, the one-dimensional model does an adequate job of modelling both subcases. Equation (3.13) predicts $H_{stop}/L = 0.05$, which, according to figure 3, is seen to be very close to the overdamped value and slightly above the underdamped value, as expected.

To compare behaviours in the continual descent regime, we choose $G = 1.9$ per (3.14), and use $V = 26$ and $\epsilon_Y = 500 \times 10^{-6}$. Figures 3 and 4(*d*) show a significant level of agreement between the results of the one-dimensional model and the full FEM simulation in this case. This example offers a stringent test of whether the model can accurately handle large deformations; as indicated in figure 4(*d*), the filament deflects about a quarter of its original length by the end of the run, and we find local strains over 23 % near the clamp. Accounting for thinning of the filament cross-section (2.9) and use of (2.6) rather than a small-strain linear formula (i.e. $s_{x_0} - 1$) are both necessary for this level of agreement; otherwise the prediction diverges early on from the FEM solutions, as we have verified with additional numerical tests.

4. Discussion

We have derived a simple one-dimensional model for thin filaments of complex fluids, valid for finite stretches and large rotations, and thus large planar deformations, by assuming a simple additive form for the decomposition of elastic and plastic strains,

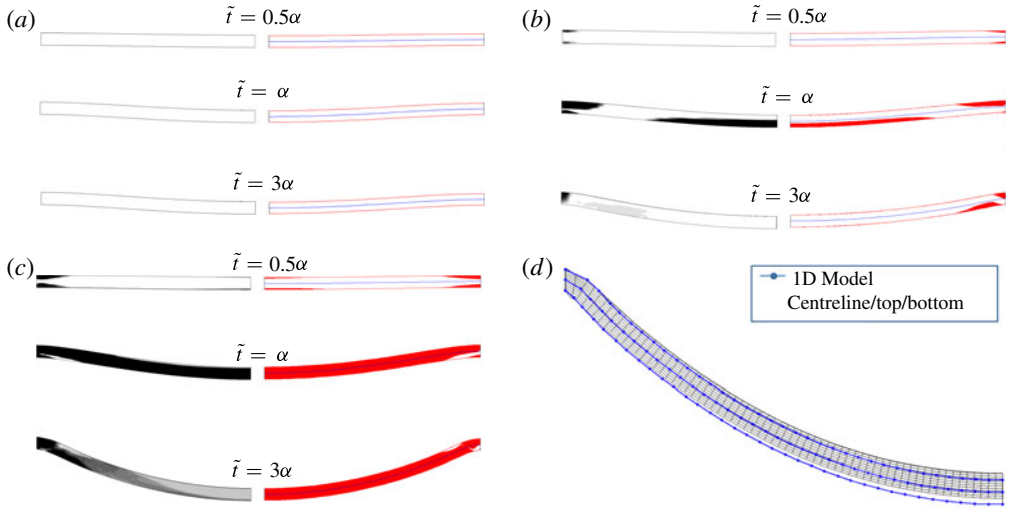

FIGURE 4. (Colour online) In each of (*a*)–(*c*), we compare snapshots of the finite element simulations (left half) to those of the reduced one-dimensional model (mirrored right half) during the initial stages of deformation where flow behaviour undergoes the most variation. The material parameters are chosen to span the regimes of (*a*) no yielding, (*b*) arrested descent (overdamped shown), and (*c*) continual descent. All finite element solutions show the field of normalized plastic shear rate $\tilde{\dot{\gamma}} = |\boldsymbol{L}^p| L\sqrt{\rho/E}$ plotted in greyscale from $0 =$ white to $4.4 \times 10^{-4} =$ black. The solutions of the one-dimensional model show the curve of the centreline and corresponding top and bottom filament surfaces, and are also shaded in wherever the linear-in-z stress field estimate utilized by (2.24) predicts the material to be exceeding σ_Y. In each, $\alpha = 46$. (*d*) Comparison of the deformed FEM mesh to the one-dimensional model prediction at $\tilde{t} = 10\alpha$ in the continual descent case.

led by previous work on the viscous and viscoelastic catenary. The resulting theory takes the form of coupled partial differential equations in one space dimension and time for the evolution of the position and plastic state fields. This is advantageous in two ways: it allows us to see transparently the various processes coupling geometry and flow, and from a computational perspective the solution of the partial differential equations represents a considerable savings over the solution of multi-dimensional bulk equations with free boundaries.

To test our theory, we considered the descent of a catenary made of a Maxwell fluid, using a combination of numerical simulation of the reduced equations and some analytical estimates. A particular outcome of this was a simple expression for the evolution of the midpoint that might be of some use in experimental rheology. We also considered the case of a yield-stress material, and identified a phase diagram for the regimes of behaviour such as the arrested and continual descent of a filament. A comparison of the simulations of our one-dimensional model to FEM solutions of fully meshed three-dimensional filaments showed that the simplified theories can capture all the different phenomena quantitatively.

A natural next step is to extend our theory to account for out-of-plane filament deformation and/or torsion for a bent, twisted filament. Furthermore, since the integrated plastic strain field variables arise naturally in our approach, we can also extend our theory to consider a viscoplastic plate theory with appropriate modifications to represent phenomena such as growth or inherent curvature. As in the filament case,

a reduced-dimensional model could provide a simplified approach for analytical and numerical studies.

Acknowledgements

K.K. thanks the NSF MSPRF for partial support. L.M. thanks the Harvard NSF - MRSEC and the MacArthur Foundation for partial support.

Appendix. Higher-order spatial approximations for plastic flow

As shown in the body of this paper, the linear-order approximation used for the z dependence of the stress when evolving P and C appears to offer sufficient accuracy. However, there are circumstances where a more precise spatial description may be necessary, as in situations of repeated and asymmetric loading and unloading under combined bending and stretching. Such actions tend to induce complex through-thickness stress and strain distributions. In these cases, the following higher-order scheme can be used, which requires additional state variables.

Letting $p_n(z)$ be the nth-order Legendre polynomial, we define the scaled functions $L_n(z) = \sqrt{(2n+1/h)}p_n(2z/h)$, which form a complete orthonormal set over $[-h/2, h/2]$, i.e. $\int_{-h/2}^{h/2} L_n L_m \,\mathrm{d}z = \delta_{mn}$. For a filament of rectangular cross-section with z-thickness h, the distributions of plastic strain and stress can thus be written as

$$\epsilon^p(z, x_0, t) = \sum_{n=0}^{\infty} a_n(x_0, t) L_n(z), \quad \sigma(z, x_0, t) = \sum_{n=0}^{\infty} b_n(x_0, t) L_n(z). \tag{A 1}$$

Given a non-Newtonian flow rule $\hat{\epsilon}_t^p(\sigma)$, we use (2.8) and orthogonality to derive

$$\frac{\partial a_n(x_0, t)}{\partial t} = \int_{-h/2}^{h/2} \hat{\epsilon}_t^p \left(E \log(s_{x_0}) - E\theta_{x_0} z - E \sum_{m=0}^{\infty} a_m(x_0, t) L_m(z)\right) L_n(z) \,\mathrm{d}z. \tag{A 2}$$

Keeping terms up to $n = k$ and truncating the sum at the kth term, the above gives a system of evolution laws for $\{a_0, \ldots, a_k\}$ that provides a kth-order spatial approximation for the plastic strain and stress. The terms we called P and C in § 2.3 are proportional to a_0 and a_1 respectively, and their evolution laws (2.12) are identically defined by the zeroth- and first-order formulae from (A 2). Thus, the case of $k = 1$ is equivalent to our original system from § 2.3. For every order of accuracy desired above first order, an additional a variable must be added to the system and evolved at all x_0 positions using the corresponding law from (A 2). This is not surprising: a better description of the plastic strain field ought to require more stored information.

REFERENCES

Brochard-Wyart, F. & de Gennes, P.-G. 2007 The viscous catenary: a poor man's approach. *Europhys. Lett.* **80** (3), 36001.

Gurtin, M., Fried, E. & Anand, L. 2010 *The Mechanics and Thermodynamics of Continua*. Cambridge University Press.

Howell, P. D. 1996 Models for thin viscous sheets. *Eur. J. Appl. Math.* **7** (4), 321–343.

Hult, J. A. 1966 *Creep in Engineering Structures*. Blaisdell Publishing Company.

Koulakis, J. P., Mitescu, C. D., Brochard-Wyart, F., de Gennes, P.-G. & Guyon, E. 2008 The viscous catenary revisited: experiments and theory. *J. Fluid Mech.* **609**, 87–110.

Kraus, H. 1980 *Creep Analysis*. Wiley.

LE MERRER, M., SEIWERT, J., QUÉRÉ, D. & CLANET, C. 2008 Shapes of hanging viscous filaments. *Europhys. Lett.* **84** (5), 56004.

RIBE, N. M. 2001 Bending and stretching of thin viscous sheets. *J. Fluid Mech.* **433**, 135–160.

ROY, A., MAHADEVAN, L. & THIFFEAULT, J.-L. 2006 Fall and rise of a viscoelastic filament. *J. Fluid Mech.* **563**, 283–292.

TEICHMAN, J. & MAHADEVAN, L. 2003 The viscous catenary. *J. Fluid Mech.* **478**, 71–80.

WANG, C. Y. & WATSON, L. T. 1982 The elastic catenary. *Intl J. Mech. Sci.* **24** (6), 349–357.

ZYLSTRA, A. & MITESCU, C. 2009 Regime transitions in the viscous catenary. *Europhys. Lett.* **87** (2), 26003.